

Synergistic bulk and surface engineering via rapid quenching for high-performance Li-rich layered manganese oxide cathodes

Xinyun Xiong(熊馨筠), Sichen Jiao(焦思晨), Qinghua Zhang(张庆华), Luyao Wang(王璐瑶), Kun Zhou(周坤), Bowei Cao(曹博维), Xilin Xu(徐熙林), Xiqian Yu(禹习谦), and Hong Li(李泓)

Citation: Chin. Phys. B, 2025, 34 (**5**): 058201. DOI: 10.1088/1674-1056/adc673
http://cpb.iphy.ac.cn; http://iopscience.iop.org/cpb

What follows is a list of articles you may be interested in

Significant increase in thermal conductivity of cathode material $LiFePO_4$ by Na substitution: A machine learning interatomic potential-assisted investigation

Shi-Yi Li(李诗怡), Qian Liu(刘骞), Yu-Jia Zeng(曾育佳), Guofeng Xie(谢国锋), and Wu-Xing Zhou(周五星)
Chin. Phys. B, 2025, 34 (**2**): 028201. DOI: 10.1088/1674-1056/ad9e99

Defect chemistry engineering of Ga-doped garnet electrolyte with high stability for solid-state lithium metal batteries

Sihan Chen(陈思汗), Jun Li(黎俊), Keke Liu(刘可可), Xiaochen Sun(孙笑晨), Jingwei Wan(万京伟), Huiyu Zhai(翟慧宇), Xinfeng Tang(唐新峰), and Gangjian Tan(谭刚健)
Chin. Phys. B, 2024, 33 (**8**): 088203. DOI: 10.1088/1674-1056/ad41b9

Surface encapsulation of layered oxide cathode material with $NiTiO_3$ for enhanced cycling stability of Na-ion batteries

Zilin Hu(胡紫霖), Bin Tang(唐彬), Ting Lin(林挺), Chu Zhang(张楚), Yaoshen Niu(牛耀申), Yuan Liu(刘渊), Like Gao(高立克), Fei Xie(谢飞), Xiaohui Rong(容晓晖), Yaxiang Lu(陆雅翔), and Yongsheng Hu(胡勇胜)
Chin. Phys. B, 2024, 33 (**8**): 088202. DOI: 10.1088/1674-1056/ad50c2

Accurate estimation of Li/Ni mixing degree of lithium nickel oxide cathode materials

Penghao Chen(陈鹏浩), Lei Xu(徐磊), Xiqian Yu(禹习谦), and Hong Li(李泓)
Chin. Phys. B, 2024, 33 (**5**): 058202. DOI: 10.1088/1674-1056/ad3036

High-throughput theoretical design of lithium battery materials

Shi-Gang Ling(凌仕刚), Jian Gao(高健), Rui-Juan Xiao(肖睿娟), Li-Quan Chen(陈立泉)
Chin. Phys. B, 2016, 25 (**1**): 018208. DOI: 10.1088/1674-1056/25/1/018208

RAPID COMMUNICATION

Synergistic bulk and surface engineering via rapid quenching for high-performance Li-rich layered manganese oxide cathodes

Xinyun Xiong(熊馨筠)[1,3], Sichen Jiao(焦思晨)[2,4], Qinghua Zhang(张庆华)[1], Luyao Wang(王璐瑶)[1,4], Kun Zhou(周坤)[1,3], Bowei Cao(曹博维)[1,3], Xilin Xu(徐熙林)[2,4], Xiqian Yu(禹习谦)[1,2,4,†], and Hong Li(李泓)[1,2,4,‡]

[1] *National Laboratory for Condensed Matter Physics, Institute of Physics, Chinese Academy of Sciences, Beijing* 100190, *China*
[2] *Beijing Frontier Research Center on Clean Energy, Huairou Division, Institute of Physics, Chinese Academy of Sciences, Beijing* 100190, *China*
[3] *School of Physical Sciences, University of Chinese Academy of Sciences, Beijing* 100049, *China*
[4] *Center of Materials Science and Optoelectronics Engineering, University of Chinese Academy of Sciences, Beijing* 100049, *China*

(Received 4 March 2025; revised manuscript received 19 March 2025; accepted manuscript online 28 March 2025)

Lithium-rich manganese-based cathodes (LRMs) have garnered significant attention as promising candidates for high-energy-density batteries due to their exceptional specific capacity exceeding 300 mAh/g, achieved through synergistic anionic and cationic redox reactions. However, these materials face challenges including oxygen release-induced structural degradation and consequent capacity fading. To address these issues, strategies such as surface modification and bulk phase engineering have been explored. In this study, we developed a facile and cost-effective quenching approach that simultaneously modifies both surface and bulk characteristics. Multi-scale characterization and computational analysis reveal that rapid cooling partially preserves the high-temperature disordered phase in the bulk structure, thereby enhancing the structural stability. Concurrently, Li^+/H^+ exchange at the surface forms a robust rock-salt/spinel passivation layer, effectively suppressing oxygen evolution and mitigating interfacial side reactions. This dual modification strategy demonstrates a synergistic stabilization effect. The enhanced oxygen redox activity coexists with the improved structural integrity, leading to superior electrochemical performance. The optimized cathode delivers an initial discharge capacity approaching 307.14 mAh/g at 0.1 C and remarkable cycling stability with 94.12% capacity retention after 200 cycles at 1 C. This study presents a straightforward and economical strategy for concurrent surface–bulk modification, offering valuable insights for designing high-capacity LRM cathodes with extended cycle life.

Keywords: lithium-rich manganese-based cathodes, surface–bulk engineering, oxygen redox activity, high-capacity cathodes, long-cycle stability

PACS: 82.47.Aa, 82.45.Fk

DOI: 10.1088/1674-1056/adc673 **CSTR:** 32038.14.CPB.adc673

1. Introduction

The on-going market demands for high-energy-density lithium-ion batteries (LIBs), driven by rapidly evolving applications in electric vehicles, portable electronics, and grid-scale energy storage systems, have created an urgent need for advanced cathode materials with superior specific capacity and operating voltage. While conventional layered ternary oxides, particularly nickel-rich layered oxide cathodes,[1–4] currently deliver energy densities of 300–400 Wh/kg that meet baseline requirements, emerging technological frontiers such as long-range electric transportation and next-generation aerial mobility systems demand a paradigm shift toward battery systems exceeding 500 Wh/kg. LRMs have emerged as a transformative solution, using concurrent cationic (transition metal, TM) and anionic (oxygen) redox reactions to achieve exceptional specific capacities surpassing 300 mAh/g.[5] However, this oxygen participation mechanism presents huge challenges, such as oxygen release,[6,7] and ensuing irreversible phase transitions through TM migration.[8,9] These structural instabilities result in unfavorable electrochemical behaviors including low initial Coulombic efficiency, progressive voltage fading, and rapid capacity degradation.[10,11]

To date, numerous strategies have been developed to address these challenges, primarily focusing on surface modification, morphological engineering, and bulk structure design. Among surface modification approaches, the most prevalent methods include surface coating, surface elemental doping, and surface reconstruction. Extensive research has been conducted on coating materials such as electronic conductors (e.g., carbon),[12] fast-ion conductors (e.g., perovskite-type compounds),[13] and polyanionic salts.[14] These coatings typically form inert protective layers that minimize direct contact between the cathode and electrolyte, thereby suppressing interfacial side reactions. Furthermore, given the inherently poor ionic/electronic conductivity of LRMs, coating design plays a dual role: electronic conductors estab-

†Corresponding author. E-mail: xyu@iphy.ac.cn
‡Corresponding author. E-mail: hli@iphy.ac.cn

© 2025 Chinese Physical Society and IOP Publishing Ltd. All rights, including for text and data mining, AI training, and similar technologies, are reserved.

lish efficient electron transport pathways to improve charge transfer kinetics, while fast-ion conductors create favorable lithium-ion diffusion channels. Both mechanisms synergistically enhance rate performance beyond merely mitigating parasitic reactions. Surface elemental doping with species such as Al^{3+},[15] Nb^{5+},[16] and Mo^{6+}[17] enhances structural stability at the cathode/electrolyte interface by strengthening oxygen bonding energy, effectively suppressing oxygen loss. This modification concurrently improves ionic/electronic conductivity, leading to significant enhancements in both cycling durability and rate capability. Surface reconstruction techniques, achieved through liquid–solid reactions (e.g., acid treatment),[18] gas–solid reactions (e.g., CO_2[19] or dual-gas CO_2/NH_3 treatments[20]), or solid-solid reactions (e.g., urea[21] or dopamine-assisted processes[22]), induce controlled delithiation to transform the surface into a spinel-like phase. This structural transformation substantially improves surface stability while maintaining electrochemical performance.

Regarding bulk structural optimization at the atomic scale, key approaches involve regulating the ordering degree of native TM cations (Ni, Co, Mn)[23] and implementing foreign element doping. Cationic dopants such as Mg^{2+},[24] Al^{3+},[25] and La^{3+},[26] along with anionic substitutions including S^{2-},[27] F^{-},[28] and PO_4^{3-},[29] have demonstrated effectiveness in optimizing crystal structure and enhancing electrochemical performance. At the lattice level, the introduction of alkali metal ions (Na^{+},[30] K^{+}[31]) has proven beneficial by expanding interlayer spacing in lithium slabs, thereby facilitating Li^{+}-ion transport. Furthermore, gradient architecture also shows enhanced lattice stability by synthesizing element concentration gradients within particles.[32,33] Multiphase composite strategies, particularly O_2/O_3 phase combinations, synergistically combine the advantages of different crystalline phases to simultaneously improve specific capacity while mitigating capacity and voltage decay.[34,35]

Conventional optimization strategies for LRMs predominantly focus on either surface modification or bulk-phase engineering, often requiring complex post-synthesis treatments. In contrast to conventional approaches, this study innovatively adapts the well-established industrial quenching technique from metallurgical practice, employing an eco-friendly ice-water mixture (0 °C) as the quenching medium. This strategy achieves simultaneous bulk-phase and surface modification of LRM while eliminating the energy-intensive water-washing step typically required in cathode production. By applying rapid thermal quenching to low-lithium-content precursors, which typically undergo thermodynamically driven phase separation and impurity formation during natural cooling,[36] we simultaneously induce partial cation disordering in the bulk TM layers and reinforce a hybrid rock-salt/spinel passivation layer at the surface. This dual modification creates a synergistic effect: enhanced structural stability balances optimized oxygen redox activity, effectively suppressing irreversible oxygen loss while mitigating cathode-electrolyte interfacial side reactions. Crucially, the approach also inhibits detrimental phase evolution (e.g., spinel/rock-salt transformations) during prolonged cycling. The optimized LRM cathode delivers an exceptional initial discharge capacity of 307.14 mAh/g and retains 94.12% capacity after 200 cycles. This study provides a scalable pathway to develop high-capacity, structurally stable LRMs for next-generation high-performance LIBs.

2. Methods

2.1. Materials synthesis

The P-LRM was synthesized via conventional solid-state reaction using stoichiometric lithium carbonate (Li_2CO_3) and transition metal carbonate precursors with a Ni:Co:Mn molar ratio of 13:13:54. The metal carbonate precursors, prepared through a co-precipitation method in the previous works,[37] underwent a multi-stage calcination protocol: initial thermal treatment at 350 °C for 6 h, followed by sequential sintering at 700 °C (15 h) and 860 °C (5 h) under atmospheric conditions, with subsequent natural cooling to ambient temperature. A series of lithium-stoichiometry variants (P-1.30 to P-1.60) were systematically prepared through precise control of Li/TM atomic ratios (1.30–1.60) while maintaining identical sintering parameters. The quenched counterparts (Q-LRM series) were synthesized using identical thermal profiles with modified cooling kinetics: Upon completing the 860 °C sintering stage, samples were rapidly transferred from the muffle furnace to an ice–water quenching medium (0 °C) using quartz crucibles, followed by immediate vacuum filtration and drying at 120 °C under reduced pressure. This controlled quenching protocol produced the Q-1.30 to Q-1.60 series, where rapid thermal arrest served as the sole experimental variable compared to their naturally cooled P-series analogs.

2.2. Materials characterization

The crystallographic properties of P-LRM and Q-LRM were investigated through x-ray diffraction (XRD, Bruker D8 Advance) employing Cu-$K\alpha$ radiation ($\lambda = 1.5405$ Å) across a 2θ range of 10°–80°, with lattice parameter refinement performed using Fullprof software. Elemental composition analysis was conducted via inductively coupled plasma spectroscopy (ICP). Surface morphology examination utilized scanning electron microscopy (SEM, Hitachi S-8400), while high-resolution transmission electron microscopy (HRTEM, JEOL JEM-F200) provided nanostructural characterization. X-ray photoelectron spectroscopy (XPS, Thermo Fisher ESCALA 250 Xi) with monochromatic Al $K\alpha$ radiation (150 W) was employed to determine surface element valence states. Specifically, manganese valence was calculated using the empirical relation $V_{\mathrm{Mn}} = 9.67 - 1.27\Delta E_{3s}$, derived from Mn 3s

orbital energy splitting.[38] Surface vibrational modes were analyzed using Raman spectroscopy (HORIBA LabRAM HR Evolution). Advanced electron microscopy characterization involved high-angle annular dark-field scanning TEM (HAADF-STEM, ARM-200CF STEM, 200 keV) coupled with electron energy loss spectroscopy (EELS). The EELS system (Gatan GIF Quantum 965) recorded Mn *L*-edge and O *K*-edge spectra at 0.3 eV/channel resolution in dual EELS mode. Gas evolution during electrochemical activation was monitored via differential electrochemical mass spectrometry (DEMS, QAS 100 DEMS). Thermal analysis was performed using the differential scanning calorimetry (DSC, Netzsch DSC 214) system with 10 °C/min heating rate. Prior to testing, 4.8V-charged cathodes underwent dimethyl carbonate washing and glovebox drying to eliminate electrolyte residues. The delithiated active material was subsequently blended with 1 M $LiPF_6$ in EC:DEC (3:7 v/v) electrolyte at 2 μL/mg mass ratio. Sample encapsulation in pressurized crucibles effectively suppressed volatilization during thermal scanning.

2.3. Electrochemical measurements

The cathode composite was formulated with 80% active material, 10% conductive carbon, and 10% PVDF binder in NMP solvent. Uniform slurry coating on aluminum foil was achieved through controlled drying at 55 °C for 6 hours, yielding electrodes with 10 mm diameter and 3–4 mg/cm^2 active mass loading. Electrochemical cells (2032-type) were assembled in an argon-filled glovebox (< 0.1 ppm O_2 & H_2O) using the prepared cathode, Al_2O_3-coated polypropylene separator, lithium anode, and commercial electrolyte (Shanshan Advanced Materials). Initial activation involved 0.1 C cycling (2.0–4.8 V, 1 C = 250 mA/g) followed by 1 C cycling stability evaluation on a LAND test system. Electrochemical characterization included cyclic voltammetry (CV, CH Instruments) at 0.1 mV/s scan rate and impedance spectroscopy (EIS, Bio-Logic SP-200) over 1 MHz–100 mHz with 5 mV AC perturbation.

2.4. Theoretical calculation

Ordered and disordered structures were modeled from the Li_2MnO_3 phase ($C2/m$) with a target chemical composition of $Li_{28}Mn_{15}Ni_5O_{48}$. The low-energy state ordered structure was constructed by enumerating all possible intralayer configurations using the Pymatgen code, followed by Ewald electrostatic energy summation. Disordered configurations were generated via the special quasirandom structure (SQS) approach implemented in the ATAT toolkit.[39] For the specified composition ($Li_{28}Mn_{15}Ni_5O_{48}$), a cluster expansion was initiated considering pair interactions up to 7.5 Å, triplet interactions within 4.5 Å, and quadruplet interactions also within 4.5 Å. All the calculations were performed using density functional theory (DFT) with the projector-augmented wave (PAW) method, as incorporated in the Vienna *Ab initio* Simulation Package (VASP).[40,41] All calculations were spin-polarized and initialized with a ferromagnetic configuration. The strongly constrained and appropriately normed (SCAN) functional was employed for structural relaxation and energy calculation,[42] until the convergence criteria for energy and force were met, set at 10^{-5} eV and 0.02 eV/Å, respectively. A cutoff energy of 520 eV was employed, with *k*-point sampling performed using the Monkhorst–Pack grid, corresponding to a density of ~ 0.02 Å^{-3}.

3. Results and discussion

The precursor with a nominal composition of $Ni_{0.16}Co_{0.16}Mn_{0.68}CO_3$ was synthesized via a coprecipitation method.[37] Subsequent high-temperature lithiation at a Li/TM molar ratio of 1.5 yielded the conventional $Li_{1.2}Ni_{0.13}Co_{0.13}Mn_{0.54}O_2$ structure. To optimize bulk and interfacial properties, we systematically adjusted the Li/TM ratio (1.30–1.60) during lithiation, generating a series of LRMs (denoted as P1.30–P1.60). Lower Li/TM ratios (< 1.50) were selected to suppress grain growth[43] and structural defects (e.g., metal site vacancies,[44] Li/Ni cation mixing,[45] lattice distortion[46]), thereby enhancing lithium-ion diffusion kinetics and stabilizing the bulk framework. Concurrently, reduced lithium content promotes the formation of a spinel/rock-salt passivation layer at the surface, which improves interfacial stability.[47]

All as-synthesized samples underwent rapid quenching in an ice-water bath (denoted as Q1.30–Q1.60). As illustrated in Fig. S1, XRD analysis revealed that Li-deficient samples (P1.30–P1.40) exhibited impurity phases attributed to thermodynamically driven phase separation during natural cooling, which has been attributed to performance degradation.[48] As depicted in Fig. S2, among pristine samples, P1.45 demonstrated optimal specific capacity and cycling stability, followed by P1.40 and P1.35 with minor impurities, while the single-phase P1.50 showed inferior performance. Remarkably, quenching treatment universally enhanced electrochemical metrics across all samples. Notably, as shown in Figs. S3 and S4, the quenched Q1.40 achieved a phase-pure structure and outperformed both its parent phase (P1.40) and the higher-Li/TM counterpart Q1.45. This improvement can be ascribed to suppressed phase separation and homogenized phase distribution, as evidenced by reduced impurity peaks in Q1.30 and Q1.35. To elucidate the mechanism behind the quenching-enhanced performance, we conducted comparative studies between the optimized quenched sample ("Q-LRM" was used to replace "Q1.40") and its unmodified counterpart ("P-LRM" was used to replace "P1.40").

3.1. Quenching-induced partial disorder in bulk phase

Figure 1(a) schematically illustrates the bulk and surface structural evolution of P-LRM transitioning into Q-LRM after quenching treatment. The quenching of P-LRM containing lithium-depleted impurity phases in the bulk phase triggers lithium extraction at the surface via H^+/Li^+ ion exchange in aqueous environments. This process generates a thicker and more robust rocksalt/spinel passivation layer on the surface while simultaneously eliminating lithium-depleted impurities in the bulk. Concurrently, a partially disordered Li/TM layered structure is introduced within the bulk phase. The synergistic interaction between the modified bulk and surface structures enhances oxygen activity while improving structural stability. Figures 1(b) and 1(c) depict schematic representations of fully ordered and disordered Li/TM arrangements in the TM layers of LRM, respectively.

To qualitatively validate the necessity of quenching-induced structural disorder, DFT calculations were performed to compare the energies of fully ordered and disordered configurations at 0 K and 1000 K using the thermodynamic relation

$$E = H - TS, \tag{1}$$

where E represents the total free energy (eV), H denotes enthalpy (eV), T is temperature (K), and S stands for entropy (eV/K). Only configuration entropy was considered herein for clarity. As demonstrated in Figs. 1(d), 1(e) and Table S1, the ordered configuration exhibits a 0.21 eV energy advantage over its disordered counterpart at 0 K, where entropy contributions become negligible and enthalpy dominates the thermodynamic landscape. This energy difference can be largely modified at elevated temperatures (1000 K), where entropy-driven stabilization reduces the energy of disordered systems by 0.10 eV, consequently narrowing the energy gap to 0.11 eV. The quenching process achieves kinetic trapping of the metastable high-temperature disordered configuration through rapid cooling, resulting in controlled disorder in the bulk phase of LRMs.[49]

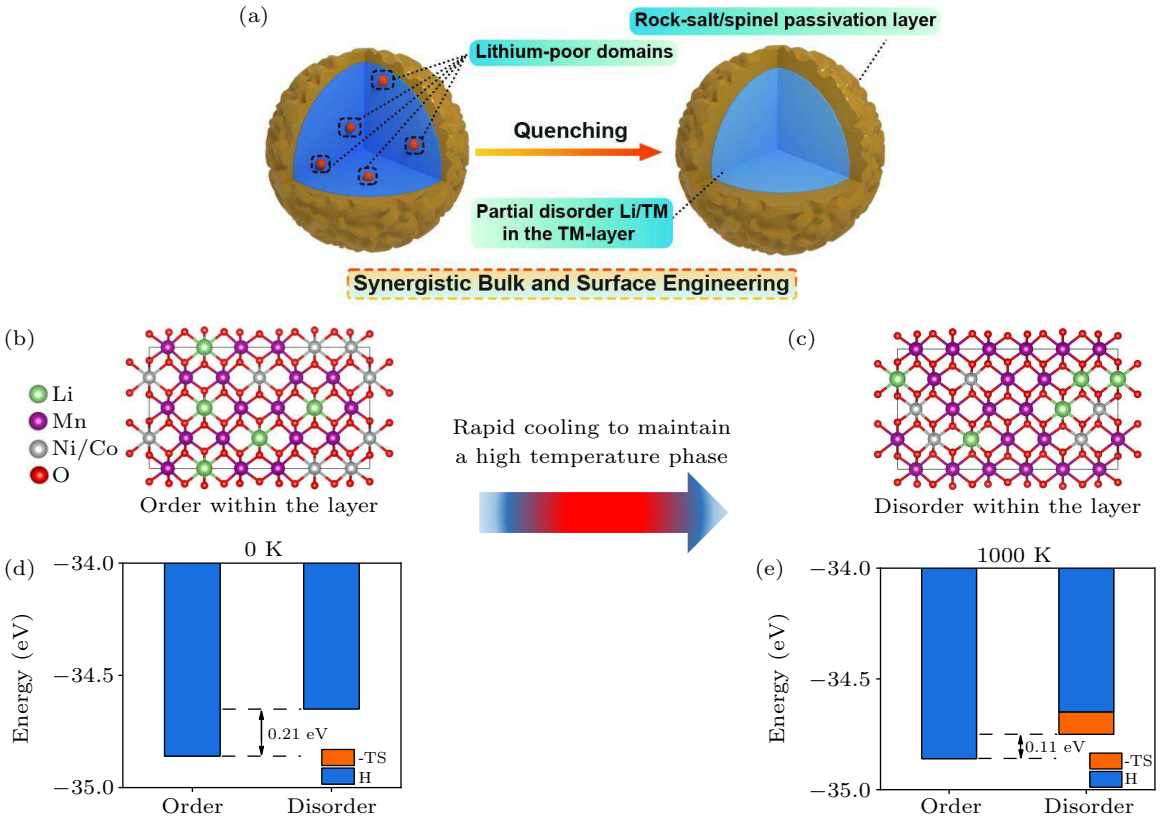


Fig. 1. (a) Schematic of the bulk and surface structures of the LRM cathode before and after quenching treatment. (b) Schematic diagram of ordered intralayer atomic arrangement in TM layers. (c) Schematic of fully disordered intralayer atomic arrangement in TM layers. (d) and (e) DFT-calculated energy differences between fully ordered and disordered Li/TM arrangements within the TM layer of LRM at 0 K and 1000 K, respectively.

3.2. Structural characterization

XRD analyses were conducted to investigate the structural evolution and lattice parameter variations between P-LRM and Q-LRM. As shown in Figs. 2(a)–2(c), all major diffraction peaks for both samples align with the α-$NaFeO_2$ structure (space group R-3m), except for three impurity peaks observed in P-LRM. The weak peaks within 20°–25° correspond to Li_2MnO_3 superlattices ($C2/m$ space group). The three additional peaks in P-LRM at 15°–17°, 28°–30°, and 35°–37° are attributed to $LiMnO_2$ ($Pmmn$), $Li_4Mn_5O_{12}$ (Fd-3m), and $LiMn_2O_4$ (Fd-3m), respectively,[44] arising from lithium deficiency-induced phase segregation during natural

cooling under thermodynamic driving forces.[36,50] Rietveld refinement of XRD patterns (Figs. 2(a), 2(b), Tables S2–S4) reveals an expanded *c*-axis parameter in the *R*-3*m* phase of Q-LRM, which facilitates lithium-ion diffusion through enhanced interlayer spacing. Magnification of the 20°–25° region (Fig. 2(d)) demonstrates reduced intensities for Li_2MnO_3 superlattice peaks $(020)_C$, $(110)_C$, and $(-111)_C$, particularly the $(110)_C$ reflection, indicating enhanced Li/Mn disorder.[23]

SEM images (Fig. S4) confirm preserved spherical secondary particle morphology (∼ 10 μm diameter) for both materials. HRTEM analyses (Figs. 2(e) and 2(f)) reveal distinct surface structural modifications. P-LRM exhibits lattice distortion near the surface with coexisting $(003)_R$ layered-phase and $(010)_P$ $LiMnO_2$ (*Pmmn*) planes, consistent with the 15°–17° impurity peak.[51] In contrast, Q-LRM maintains a pristine layered structure. HAADF-STEM imaging (Figs. 2(g) and 2(h)) was employed to probe the atomic configurations. The *Z*-contrast mechanism enables clear differentiation, where TM columns appear bright, while Li columns remain dark.[52] P-LRM displays ordered "bright–bright–dark" TM–TM–Li configurations (Fig. 2(g)), characteristic of well-ordered Li_2MnO_3 domains, as confirmed by intensity line profiles. Q-LRM exhibits randomized Li/TM distributions (Fig. 2(h)) with partial TM occupation at 2b Li sites and Li occupation at 4g TM sites, evidenced by disordered intensity profiles. This TM-layer disordering enhances thermodynamic stability and Li^+ diffusion kinetics, synergistically improving structural resilience and electrochemical performance.[23]

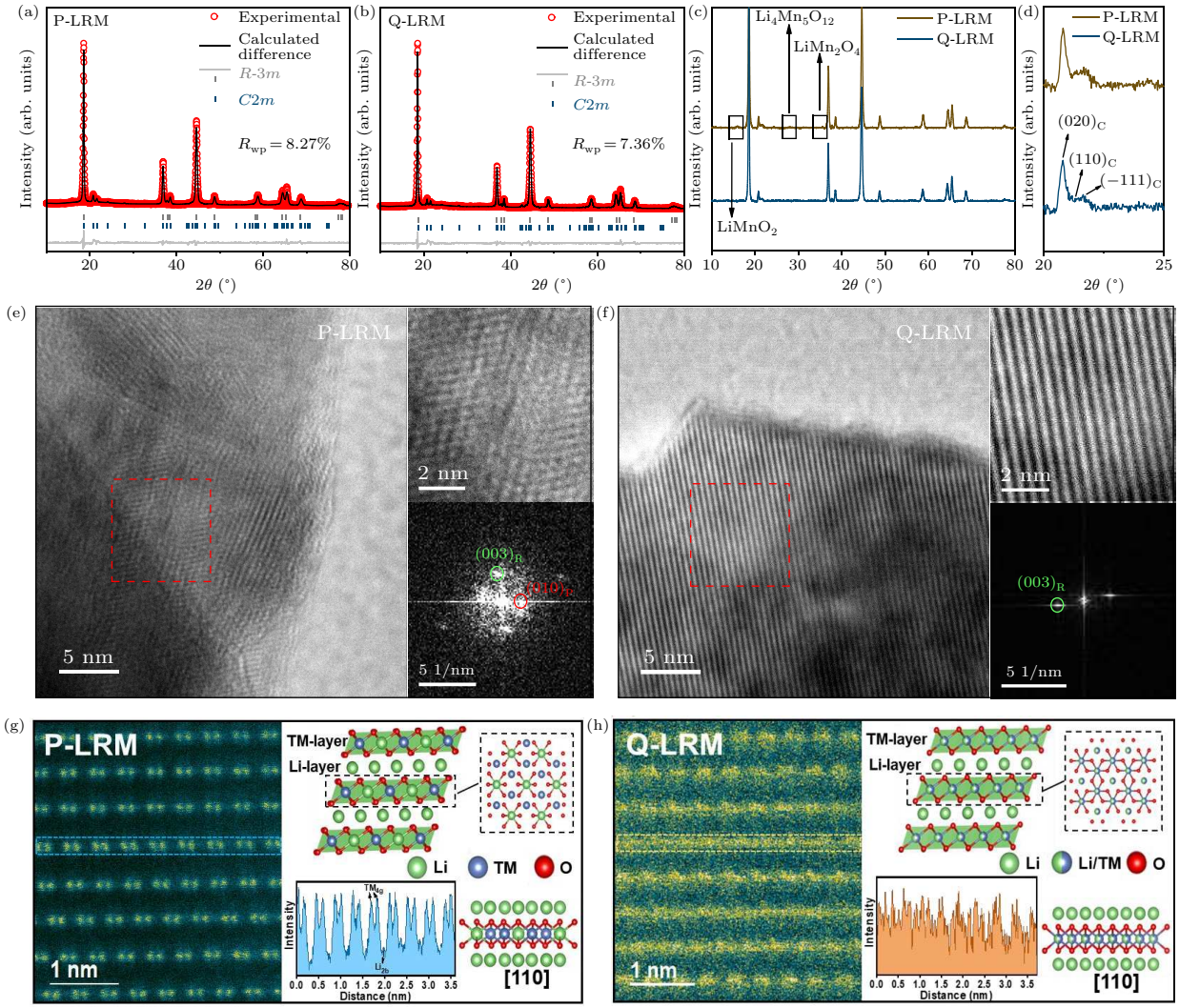


Fig. 2. Structural characterization of P-LRM and Q-LRM. (a) and (b) Rietveld refinement profiles of XRD patterns for (a) P-LRM and (b) Q-LRM. (c) Comparative XRD patterns of P-LRM and Q-LRM. (d) Magnified view of (c) in the 20°–25° range. (e) and (f) HRTEM images of (e) P-LRM and (f) Q-LRM; insets show enlarged regions and corresponding FFT patterns. (g) and (h) HAADF-STEM images along the $[110]_C$ zone axis for (g) P-LRM and (h) Q-LRM; insets display structural schematics and intensity line profiles.

3.3. Multiscale surface analysis

Following the bulk structural analysis, we conducted comprehensive surface characterization to elucidate the surface structural evolution induced by quenching. HAADF-STEM imaging along the [010] zone axis reveals distinct surface structures between P-LRM and Q-LRM (Figs. 3(a) and 3(b)). While both materials maintain bulk layered characteristics, significant differences occur within the 5 nm sur-

face region. P-LRM exhibits a 1 nm thick rocksalt/spinel composite layer at the surface, as evidenced by the corresponding FFT pattern (Fig. 3(a)). This surface reconstruction originates from lithium carbonate decomposition during synthesis.[47] In contrast, Q-LRM develops an extended ~ 4 nm disordered rocksalt/spinel structure through ice-water quenching, as confirmed by combined STEM imaging and FFT analysis of the surface region (Fig. 3(b)). The thickened inert layer effectively stabilizes lattice oxygen while suppressing surface parasitic reactions.[53] The lithium depletion mechanism was investigated through ICP measurements (Fig. S5 and Table S6), showing reduced Li/TM ratios in quenched samples. Given identical precursors and synthesis conditions, this lithium loss exclusively occurs at the surface through Li^+/H^+ exchange during rapid quenching. The resultant lithium vacancies facilitate TM cation migration, promoting the formation of a stabilized surface structure.[54] Raman spectroscopy further deciphers the short-range ordering within surface structures (Figs. 3(c) and 3(d)). Deconvolution of vibrational modes identifies three coexisting phases: (1) the layered *R*-3*m* phase (483 cm^{-1} E_g bending mode, 591 cm^{-1} A_{1g} stretching mode); (2) *C*2/*m* Li_2MnO_3 component (413 cm^{-1} A_g mode); (3) *Fd*-3*m* spinel structure (657 cm^{-1} A_{1g} Mn–O vibration).[55] Notably, Q-LRM demonstrates enhanced A_{1g} mode intensity at 657 cm^{-1}, reflecting increased spinel phase proportion. A systematic 5–8 cm^{-1} blue shift across Raman peaks suggests bond contraction and compressive stress within the reconstructed surface layer, consistent with its thickened architecture.[56]

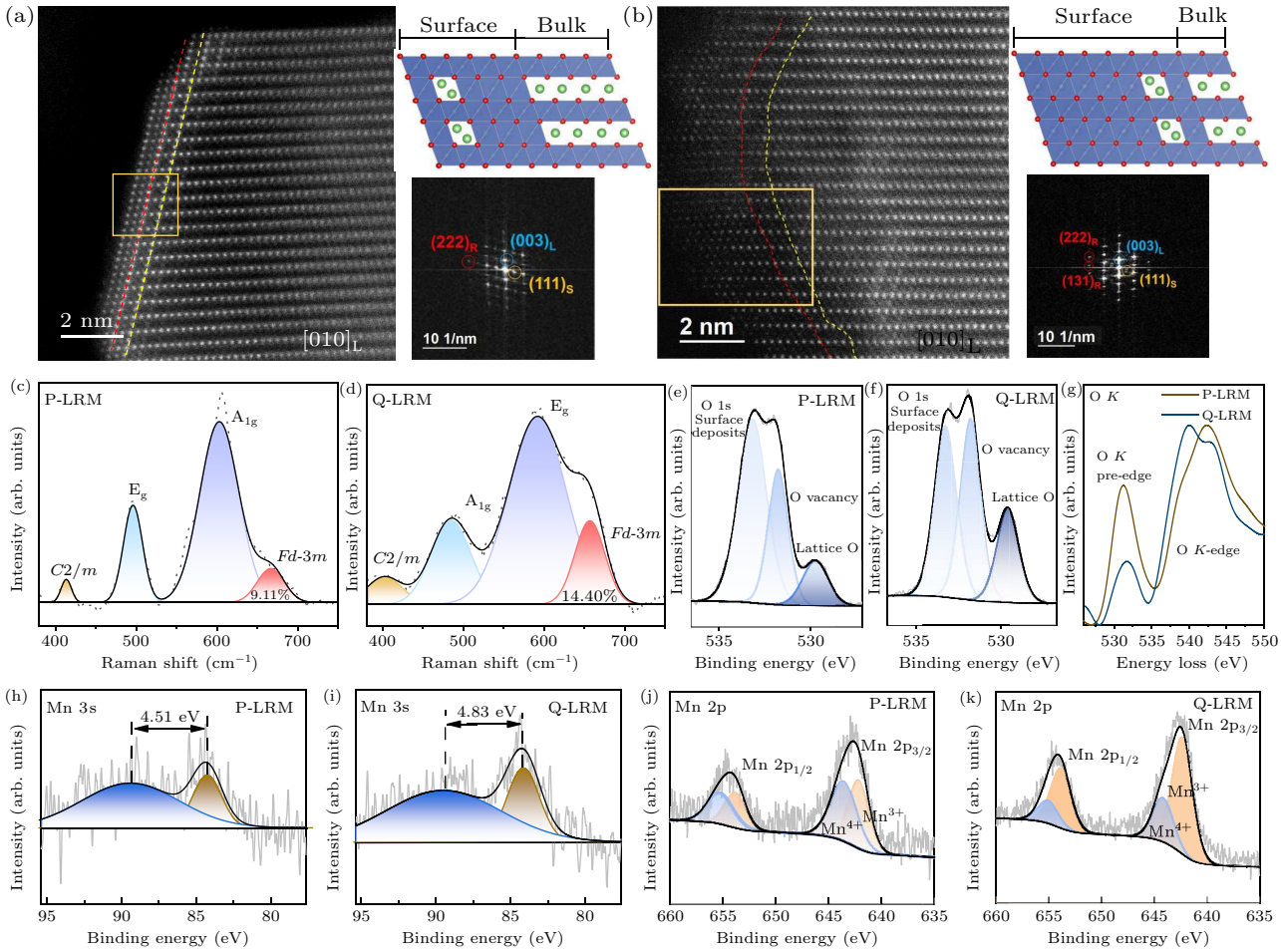


Fig. 3. Multiscale characterization of P-LRM and Q-LRM. (a), (b) HAADF-STEM images along the [010] zone axis for (a) P-LRM and (b) Q-LRM; insets show structural models and FFT patterns. (c) and (d) Raman spectra of (c) P-LRM and (d) Q-LRM (380–750 cm^{-1} range). (e) and (f) XPS O 1s spectra for (e) P-LRM and (f) Q-LRM. (g) EELS O *K*-edge spectra comparison. (h) and (i) Mn 3s XPS spectra of (h) P-LRM and (i) Q-LRM. (j) and (k) Mn 2p XPS spectra for (j) P-LRM and (k) Q-LRM.

Complementary XPS and EELS analyses reveal critical changes in surface chemistry (Figs. 3(e)–3(k)). The O 1s spectra (Figs. 3(e) and 3(f)) show increased oxygen vacancy concentration in Q-LRM, indicative of weakened TM 3d–O 2p hybridization.[57] This is corroborated by EELS O *K*-edge spectra (Fig. 3(g)), where the diminished pre-edge peak intensity (530–535 eV) confirms reduced TM–O covalency.[26] Mn valence state analysis through 3s splitting energy demonstrates a decrease from +3.94 in P-LRM (4.51 eV splitting) to +3.54 in Q-LRM (4.83 eV splitting, Figs. 3(h) and 3(i)) (the

equation can be found in Section 2).[38] Concurrently, Mn 2p spectra (Figs. 3(j) and 3(k)) reveal elevated Mn^{3+} content, suggesting surface enrichment of low-valent spinel phases (e.g., $LiMn_2O_4$). Figure S6 presents the EELS characterization of the surface (2 nm) and bulk (10 nm) regions of P-LRM and Q-LRM. The valence state of Mn is typically determined by the ratio of Mn *L*-edge L_3 to L_2.[19] As shown in Fig. S6(a), the increased L_3/L_2 ratio on the treated surface indicates a reduction in the Mn valence state, suggesting the occurrence of reduction. This phenomenon may be attributed to surface lithium deficiency and elevated oxygen valence state, which is consistent with the XPS results. Figure S6(b) demonstrates that analysis of the original Ni *L*-edge and Co *L*-edge reveals no peak shifts in either the surface or bulk phases of P-LRM. However, Q-LRM exhibits a slight shift of peaks towards lower energy, indicating a reduction in the valence states of Ni and Co in Q-LRM. The decrease in TM valence states is associated with the formation of a surface disordered phase, providing further evidence from the perspective of electronic valence states for the generation of the surface disordered phase.[58] These changes in oxygen coordination and manganese oxidation state collectively contribute to enhanced oxygen retention and structural stability.[54]

3.4. Oxygen activity and structural stability

To systematically evaluate the evolution of oxygen activity and structural stability, comprehensive investigations combining theoretical calculations, electrochemical characterization, *in situ* DEMS, and DSC were conducted on both P-LRM and Q-LRM. DFT calculations reveal enhanced oxygen redox activity in Q-LRM, as evidenced by the elevated density of states (DOS) near the Fermi level in O 2p orbitals (Fig. 4(a)). CV profiles (Fig. 4(b)) demonstrate intensified oxidation peaks above 4.5 V corresponding to $O^{2-}/O^{(2-n)-}$ redox reactions in Q-LRM, with a reduced oxygen oxidation onset potential (4.66 V vs. 4.69 V for P-LRM), while Q-LRM demonstrates a higher first-cycle reduction peak potential than that of P-LRM. These observations suggest that Q-LRM not only facilitates the reduction of oxygen redox activation potential but also effectively mitigates the oxygen-induced voltage hysteresis.[15,59] Analysis of dQ/dV curves over 200 cycles (Fig. S7) reveals sustained enhancement in both TM redox activity (below 4.4 V) and oxygen redox reversibility, synergistically contributing to superior capacity retention and cycling stability.[60] Critical stability assessments through *in situ* DEMS (0.1 C initial cycle) show significantly suppressed O_2 and CO_2 evolution in Q-LRM (Fig. 4(c)),

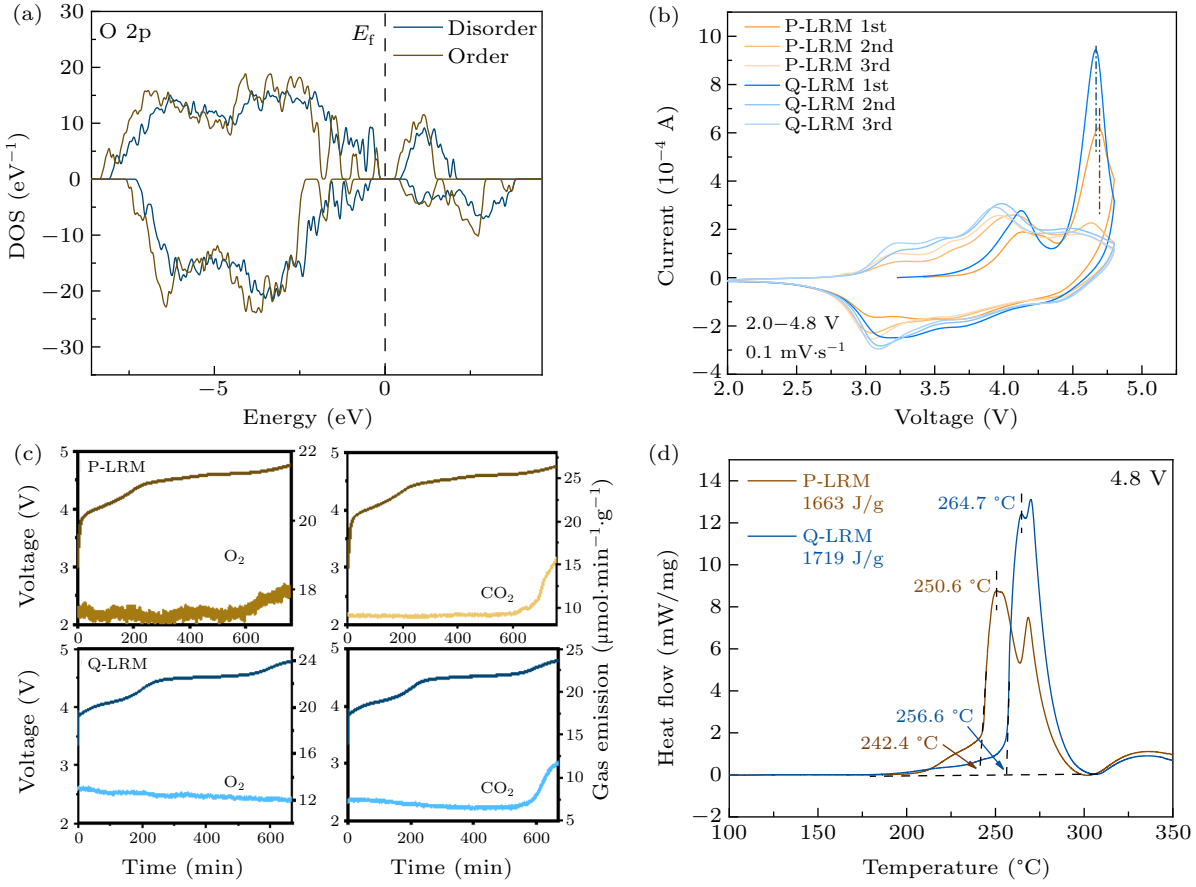


Fig. 4. (a) DFT-calculated O 2p DOS plots of P-LRM and Q-LRM. (b) CV curves of P-LRM and Q-LRM tested at 0.1 mV·s^{-1} between 2 V and 4.8 V. (c) *In situ* DEMS profiles of P-LRM and Q-LRM during the first-cycle charge at 0.1 C (1 C = 250 mA·g^{-1}, 2–4.8 V). (d) DSC analysis of delithiated P-LRM and Q-LRM charged to 4.8 V.

indicating enhanced electrochemical compatibility with electrolytes despite increased oxygen activity. DSC thermograms quantitatively demonstrate improved thermal resilience: Q-LRM exhibits a delayed exothermic onset temperature (256.6 °C vs. 242.4 °C for P-LRM) and reduced total heat release (1663 J·g^{-1} vs. 1719 J·g^{-1}). These improvements stem from dual bulk-surface modifications that simultaneously stabilize lattice oxygen through cation disordering while passivating surface reactive sites. Collectively, Q-LRM achieves an optimal balance between high oxygen redox activity, structural integrity, and thermal safety.

3.5. Electrochemical performance evaluation

To investigate the impact of quenching treatment on the electrochemical performance of LRM, a series of electrochemical tests were conducted. Initial charge–discharge profiles at 0.1 C within the voltage range of 2.0–4.8 V are shown in Fig. 5(a). The profiles exhibit two distinct regions: TM oxidation below 4.5 V and oxygen redox activity above 4.5 V.[61] The Q-LRM demonstrates a higher initial discharge capacity of 307.4 mAh·g^{-1} compared to 292.2 mAh·g^{-1} for P-LRM. The enhanced capacity below 4.5 V correlates with improved TM redox activity, which is consistent with previous structural analyses. The shortened high-voltage plateau and reduced oxygen over-oxidation contribute to increased Coulombic efficiency (92.15% vs. 85.15%), attributed to the enhanced reversibility of lattice oxygen redox and the suppressed surface oxygen loss. Cycling performance at 1 C (Fig. 5(b)) reveals significantly improved stability for Q-LRM, retaining 94.12% capacity after 200 cycles versus 89.94% for P-LRM. Furthermore, the critical challenge of voltage decay in LRMs, which hinders commercialization, is notably mitigated in Q-LRM (Fig. 5(c)). This suppression likely stems from inhibited structural evolution and TM migration. Rate capability tests (Fig. 5(d)) demonstrate superior kinetics in Q-LRM across varying current densities (0.1 C to 5 C), resulting from synergistic effects of bulk partial disorder, surface spinel phase formation, and oxygen vacancy generation. The expanded Li layer spacing induced by in-plane disordering enhances Li^+ transport kinetics, while surface oxygen vacancies and the three-dimensional channels of the spinel phase provide additional lithiation sites and faster ion diffusion pathways.[54,62]

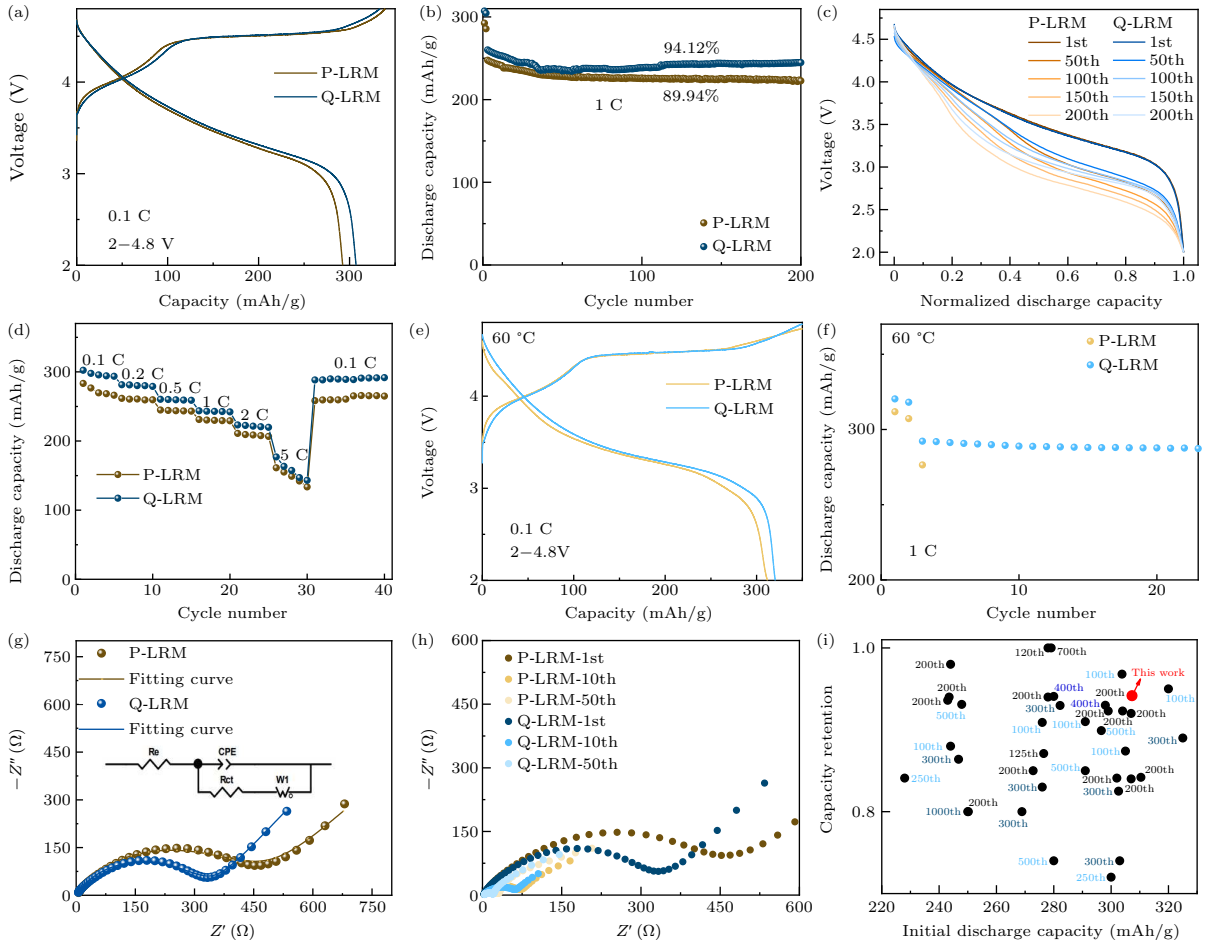


Fig. 5. Electrochemical performance evaluation. (a) Initial charge/discharge profiles at 0.1 C. (b) Cycling stability at 1 C under room temperature. (c) Normalized capacity differential curves during discharge. (d) Rate capability across various current densities. (e) High-temperature (60 °C) charge/discharge profiles at 0.1 C. (f) Elevated-temperature cycling performance at 1 C. (g) Nyquist plots of EIS after initial activation, with inset showing the equivalent circuit model. (h) Evolution of EIS spectra at selected cycles (1st, 10th, 50th). (i) Comparative evaluation of electrochemical performance between this work and reported representative modified LRMs.

Elevated-temperature evaluations at 60 °C (Figs. 5(e) and 5(f)) highlight Q-LRM's thermal stability, delivering a 320.34 mAh·g^{-1} initial discharge capacity at 0.1 C and maintaining 98.32% capacity retention at 1 C. In contrast, P-LRM suffers rapid failure due to severe electrolyte decomposition and interfacial side reactions.

EIS analysis (Figs. 5(g) and 5(h)) confirms Q-LRM's optimized kinetics, with lower interfacial resistance (R_e = 2.101 Ω) and charge transfer resistance (R_{ct} = 285.8 Ω) compared to P-LRM (2.665 Ω and 366.5 Ω, respectively). It is well-established that conventional bulk-disordered materials typically exhibit poor lithium-ion transport properties.[63] However, the bulk structural disorder introduced in this study is specifically partial and confined to transition metal (TM) layers. This controlled disorder, combined with the creation of additional lithium vacancies,[64] synergistically enhances the lithium-ion mobility. Furthermore, the three-dimensional spinel-like surface channels contribute to improved ionic transport pathways.[53] These combined modifications collectively result in reduced ohmic resistance (R_e) and charge transfer resistance (R_{ct}) in the treated samples, as evidenced by electrochemical impedance measurements. The impedance evolution during cycling further validates Q-LRM's structural stability against ion-blocking phase formation. A comparative analysis with state-of-the-art modified LRMs (Fig. 5(i), Table S7) positions Q-LRM as a leading candidate, surpassing most reported systems in both initial capacity (> 300 mAh·g^{-1}) and cycling stability. In addition, compared to existing modified LRM materials, this system exhibits advantages in voltage attenuation control, with a measured decay rate of 1.306 mV/cycle. Furthermore, it compares favorably with most Co-free LRMs that typically demonstrate better voltage stability performance (Fig. S10 and Table S7). This performance breakthrough originates from the synergistic effects of bulk and surface modifications: partial Li/TM disordering in the bulk enhances structural stability while preserving oxygen redox activity, whereas the rocksalt/spinel composite surface layer suppresses TM dissolution and irreversible oxygen loss. Concurrently, expanded interlayer spacing and three-dimensional surface channels synergistically accelerate Li^+ diffusion. These collective bulk-surface optimizations provide new insight into the design of high-performance lithium-rich cathodes with balanced energy density and durability.

3.6. Structural and interfacial evolution analysis

To further elucidate the working mechanism of quenching treatment and its impact on electrochemical behavior, comprehensive investigations were conducted on the bulk structural evolution and interfacial dynamics of P-LRM and Q-LRM. Operando XRD analysis during the initial charge–discharge cycle (Figs. 6(a) and 6(b)) reveals distinct structural evolution patterns. During charging, continuous lithium extraction from the lithium layer intensifies interlayer

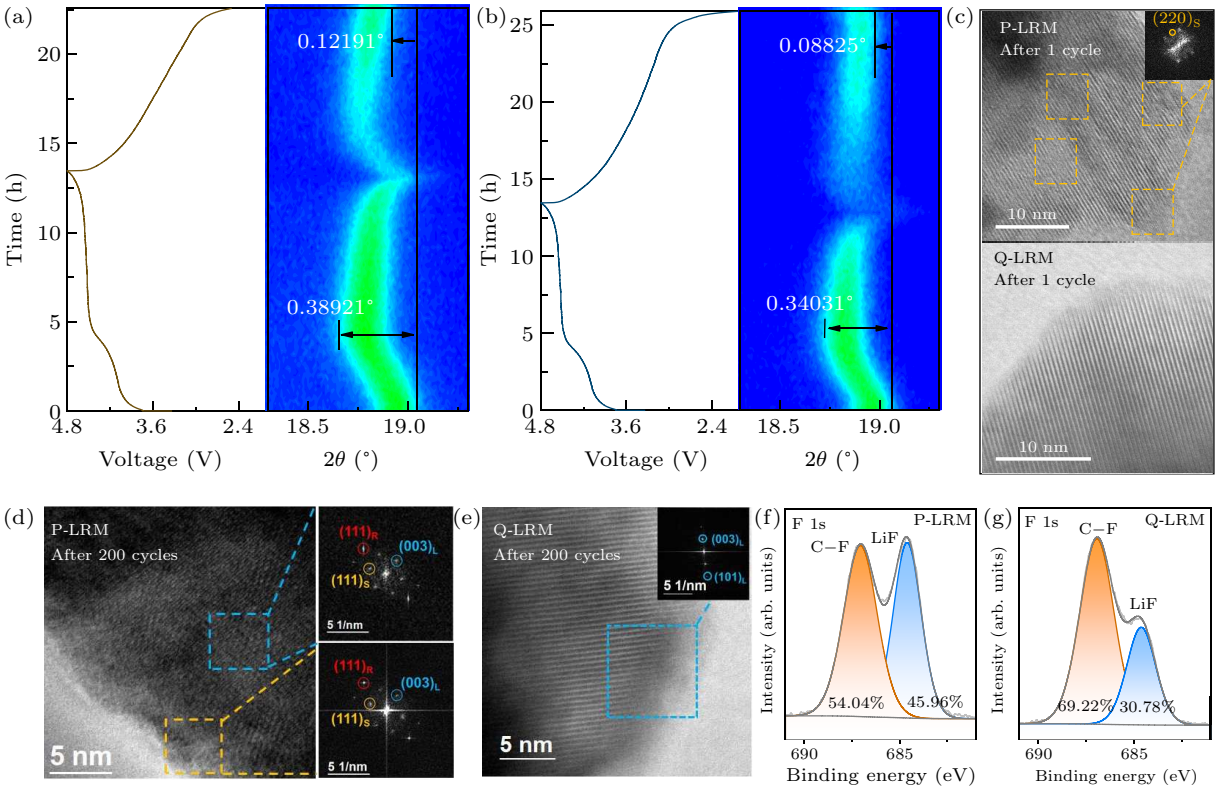


Fig. 6. Structural and interfacial evolution analysis. (a)–(b) Operando XRD patterns with corresponding galvanostatic profiles of P-LRM and Q-LRM during initial cycling. (c) Representative TEM images after 1st charge/discharge cycle. (d)–(e) Post-cycling TEM characterization after 200 cycles. (f)–(g) Comparative F 1s XPS spectra after 200 cycles.

electrostatic repulsion, expanding the interlayer spacing as evidenced by the low-angle shift of the (003) peak (18.5°–19.5°). Subsequent oxygen activation at higher voltages triggers cation migration from TM layers to lithium layers, contracting interlayer spacing and causing a high-angle (003) peak shift.[38,62] Notably, Q-LRM exhibits significantly reduced (003) peak displacement compared to P-LRM throughout the first cycle, indicating enhanced lattice rigidity that accommodates lithium intercalation with minimized structural distortion, thereby suppressing irreversible phase transitions during prolonged cycling. Post-cycling TEM characterization (Fig. 6(c)) demonstrates superior structural integrity in Q-LRM after the first cycle, maintaining a well-defined layered morphology compared to the spinel formation in P-LRM. After 200 cycles (Figs. 6(d) and 6(e)), P-LRM exhibits a thick spinel-like layer, while Q-LRM preserves a near-surface layered structure beneath a thin amorphous coating. Complementary *ex situ* XRD analysis (Fig. S8) confirms accelerated degradation in P-LRM: significant (003) peak shift and emergence of spinel (101) shoulder contrast with diminished (107) peak intensity, whereas Q-LRM retains stable crystallinity with minimal peak shift. XPS analysis of cycled electrodes (Figs. 6(f), 6(g), and S9) provides interfacial insights. Q-LRM shows attenuated Li–F signals and enhanced C–F bonding in F 1s spectra, indicating suppressed electrolyte decomposition.[65] Mn 2p spectra reveal severe manganese dissolution in P-LRM (peak intensity loss) compared to the preserved TM coordination in Q-LRM. These findings collectively demonstrate that quenching modification simultaneously enhances bulk stability and interfacial compatibility.

4. Conclusion and perspectives

In summary, this study demonstrates a facile and cost-effective strategy for concurrent bulk–surface modification of LRMs, effectively eliminating lithium-deficient secondary phases while significantly enhancing specific capacity (307.4 mAh·g^{-1} vs. 292.2 mAh·g^{-1}) and cycling stability (94.12% vs. 89.94% retention after 200 cycles). Systematic characterization and computational analysis reveal that the one-step bulk-surface modifications preserve oxygen redox activity while maintaining structural stability. Specifically, partial Li/TM disordering within the bulk structure enhances oxygen redox reversibility while stabilizing the lattice framework. Meanwhile, a rocksalt/spinel composite surface layer effectively suppresses interfacial side reactions, mitigates surface oxygen loss, and inhibits near-surface phase transformations, thereby reinforcing structural integrity. This dual-modification design strategy resolves the longstanding trade-off between high capacity and structural degradation, offering new insights for designing next-generation high-energy-density cathode materials.

Data availability statement

The data that support the findings of this study are openly available in Science Data Bank at the following link https://doi.org/10.57760/sciencedb.j00113.00235.

Acknowledgments

Project supported by the National Key Research and Development Program of China (Grant No. 2022YFB2502200) and the National Natural Science Foundation of China (Grant Nos. 52325207, 22239003, and 22393904).

References

[1] Han Q, Yu H, Cai L, Chen L, Li C and Jiang H 2024 *Proc. Natl. Acad. Sci. USA* **121** e2317282121
[2] Wang S, Liang K, Zhao H, Wu M, He J, Wei P, Ding Z, Li J, Huang X and Ren Y 2025 *Nat. Commun.* **16** 1
[3] Guo W, Wei W, Zhu H, Hu Y, Jiang H and Li C 2023 *eScience* **3** 100082
[4] Zhou X, Hong F, Wang S, Zhao T, Peng J, Zhang B, Fan W, Xing W, Zuo M, Zhang P, Zhou Y, Lv G, Zhong Y, Hua W and Xiang W 2024 *eScience* **4** 100276
[5] Assat G and Tarascon J M 2018 *Nat. Energy* **3** 373
[6] Sathiya M, Abakumov A M, Foix D, Rousse G, Ramesha K, Sauban'ere M, Doublet M L, Vezin H, Laisa C P, Prakash A S, Gonbeau D, VanTendeloo G and Tarascon J M 2015 *Nat. Mater.* **14** 230
[7] Qian D, Xu B, Chi M and Meng Y S 2014 *Phys. Chem. Chem. Phys.* **16** 14665
[8] Gu M, Belharouak I, Zheng J, Wu H, Xiao J, Genc A, Amine K, Thevuthasan S, Baer D R, Zhang J G, Browning N D, Liu J and Wang C 2013 *ACS Nano* **7** 760
[9] Hu E, Yu X, Lin R, Bi X, Lu J, Bak S, Nam K W, Xin H L, Jaye C, Fischer D A, Amine K and Yang X Q 2018 *Nat. Energy* **3** 690
[10] McColl K, Coles S W, Zarabadi-Poor P, Morgan B J and Islam M S 2024 *Nat. Mater.* **23** 826
[11] Yan P, Zheng J, Tang Z K, Devaraj A, Chen G, Amine K, Zhang J G, Liu L M and Wang C 2019 *Nat. Nanotechnol.* **14** 602
[12] Li Z, Cao S, Chen J, Wu L, Chen M, Ding H, Wang R, Guo W, Bai Y, Liu M and Wang X 2024 *Small* **20** 2400641
[13] Wei H, Huang Y, Tang L, Yan C, He Z, Mao J, Dai K, Wu X, Jiang J and Zheng J 2021 *Nano Energy* **88** 106288
[14] Yang S, Wang P, Wei H, Tang L, Zhang X, He Z, Li Y, Tong H and Zheng J 2019 *Nano Energy* **63** 103889
[15] Li S, Yang L, Liu Z, Zhang C, Shen X, Gao Y, Kong Q, Hu Z, Kuo C Y, Lin H J, Chen C T, Yang Y, Ma J, Hu Z, Wang X, Yu R, Wang Z and Chen L 2023 *Energy Storage Mater.* **55** 356
[16] Liu S, Liu Z, Shen X, Li W, Gao Y, Banis M N, Li M, Chen K, Zhu L, Yu R, Wang Z, Sun X, Lu G, Kong Q, Bai X and Chen L 2018 *Surf. Adv. Energy Mater.* **8** 1802105
[17] Geng K Q, Yang M Q, Meng J X, Zhou L F, Wang Y Q, Dmytro S, Zhang Q, Zhong S W and Ma Q X 2022 *Tungsten* **4** 323
[18] Guo W, Zhang C, Zhang Y, Lin L, He W, Xie Q, Sa B, Wang L and Peng D 2021 *Adv. Mater.* **33** 2103173
[19] Qiu B, Zhang M, Wu L, Wang J, Xia Y, Qian D, Liu H, Hy S, Chen Y, An K, Zhu Y, Liu Z and Meng Y S 2016 *Nat. Commun.* **7** 12108
[20] Yang Y, Zhu Q, Yang J, Liu H, Ren Y, Sui X, Wang P, Sun G and Wang Z 2023 *Adv. Funct. Mater.* **33** 2304979
[21] Ding X, Luo D, Cui J, Xie H, Ren Q and Lin Z 2020 *Angew Chem Int Ed* **59** 7778
[22] Ku L, Cai Y, Ma Y, Zheng H, Liu P, Qiao Z, Xie Q, Wang L and Peng D L 2019 *Chem. Eng. J.* **370** 499
[23] Jiang Y, Yu F, Que L, Deng L, Xia Y, Ke W, Han Y and Wang Z 2021 *ACS Energy Lett.* **6** 3836
[24] Song J, Ning F, Zuo Y, Li A, Wang H, Zhang K, Yang T, Yang Y, Gao C, Xiao W, Jiang Z, Chen T, Feng G and Xia D 2023 *Adv. Mater.* **35** 2208726
[25] Li Z, Li Y, Zhang M, Yin Z, Yin L, Xu S, Zuo C, Qi R, Xue H, Hu J, Cao B, Chu M, Zhao W, Ren Y, Xie L, Ren G and Pan F 2021 *Adv. Energy Mater.* **11** 2101962

[26] Zhang C, Wei B, Wang M, Zhang D, Uchiyama T, Liang C, Chen L, Uchimoto Y, Zhang R, Wang P and Wei W 2022 *Energy Storage Mater.* **46** 512

[27] Zhang K, Qi J, Song J, Zuo Y, Yang Y, Yang T, Chen T, Liu X, Chen L and Xia D 2022 *Adv. Mater.* **34** 2109564

[28] Sun X, Qin C, Zhao B, Jia S, Wang Z, Yang T, Liu X, Pan L, Zheng L, Luo D and Zhang Y 2024 *Energy Storage Mater.* **70** 103559

[29] Zhao Y, Liu J, Wang S, Ji R, Xia Q, Ding Z, Wei W, Liu Y, Wang P and Ivey D G 2016 *Adv. Funct. Mater.* **26** 4760

[30] Zheng C, Feng J, Zhang D, Zhang D and Li J 2024 *ACS Energy Lett.* **9** 1339

[31] Peng Y, Wu L, Li C F, Luo B C, Feng X Y, Hu Z Y, Li Y and Su B L 2023 *Electrochimica Acta* **454** 142390

[32] Wu T, Liu X, Zhang X, Lu Y, Wang B, Deng Q, Yang Y, Wang E, Lyu Z, Li Y, Wang Y, Lyu Y, He C, Ren Y, Xu G, Sun X, Amine K and Yu H 2021 *Adv. Mater.* **33** 2001358

[33] Wu T, Zhang X, Wang Y, Zhang N, Li H, Guan Y, Xiao D, Liu S and Yu H 2023 *Adv. Funct. Mater.* **33** 2210154

[34] Li F, Li J C, Gong M S, Lin Z Z, Chang X M, Dong M H and Hou P Y 2025 *Rare Met.*

[35] Chen Y, Liu Y, Zhang J, Zhu H, Ren Y, Wang W, Zhang Q, Zhang Y, Yuan Q, Chen G X, Gallington L C, Li K, Liu X, Wu J, Liu Q and Chen Y 2022 *Energy Storage Mater.* **51** 756

[36] McCalla E, Rowe A W, Brown C R, Hacquebard L R P and Dahn J R 2013 *J. Electrochem. Soc.* **160** A1134

[37] Huang L, Liu L, Wu H, Wang Y, Liu H and Zhang Y 2019 *J. Alloys Compd.* **775** 921

[38] Wang L, Xu L, Xue W, Fang Q, Liu H, Liu Y, Zhou K, Li Y, Wang X, Wang X, Yang X, Yu X and Wang X 2024 *Nano Energy* **121** 109241

[39] van de Walle A 2009 *Calphad* **33** 266

[40] Kresse G and Furthmüller J 1996 *Comput. Mater. Sci.* **6** 15

[41] Blöchl P E 1994 *Phys. Rev. B* **50** 17953

[42] Sun J, Ruzsinszky A and Perdew J P 2015 *Phys. Rev. Lett.* **115** 036402

[43] Zhang Y, Yin C, Qiu B, Chen G, Shang Y and Liu Z 2022 *Energy Storage Mater.* **53** 763

[44] Shunmugasundaram R, Senthil Arumugam R and Dahn J R 2015 *Loss Chem. Mater.* **27** 757

[45] Liu P, Zhang H, He W, Xiong T, Cheng Y, Xie Q, Ma Y, Zheng H, Wang L, Zhu Z Z, Peng Y, Mai L and Peng D L 2019 *J. Am. Chem. Soc.* **141** 10876

[46] Wang N, Chen Y, Yin J, Yan W, Li F and Jin Y 2022 *J. Alloys Compd.* **900** 163549

[47] Hao Z, Sun H, Ni Y, Yang G, Yang Z, Hao Z, Wang R, Yang P, Lu Y, Zhao Q, Xie W, Yan Z, Zhang W and Chen J 2024 *Adv. Mater.* **36** 2307617

[48] Shunmugasundaram R, Senthil Arumugam R, Harris K J, Goward G R and Dahn J R 2016 *Chem. Mater.* **28** 55

[49] Aktekin B, Massel F, Ahmadi M, Valvo M, Hahlin M, Zipprich W, Marzano F, Duda L, Younesi R, Edström K and Brandell D 2020 *ACS Appl. Energy Mater.* **3** 6001

[50] McCalla E, Rowe A W, Camardese J and Dahn J R 2013 *Chem. Mater.* **25** 2716

[51] Reimers J N, Fuller E W, Rossen E and Dahn J R 1993 *J. Electrochem. Soc.* **140** 3396

[52] Findlay S D, Shibata N, Sawada H, Okunishi E, Kondo Y and Ikuhara Y 2010 *Ultramicroscopy* **110** 903

[53] Gou X, Hao Z, Hao Z, Yang G, Yang Z, Zhang X, Yan Z, Zhao Q and Chen J 2022 *Adv. Funct. Mater.* **32** 2112088

[54] Zeng L, Liang H, Wang Y, Ying X, Qiu B, Pan J, Zhang Y, Wen W, Wang X, Gu Q, Li J, Shi K, Shen Y, Liu Q and Liu Z 2025 *Energy Environ. Sci.* **18** 284

[55] Luo D, Ding X, Fan J, Zhang Z, Liu P, Yang X, Guo J, Sun S and Lin Z 2020 *Angewandte Chemie International Edition* **59** 23061

[56] Zhang X, Shi J, Liang J, Yin Y, Zhang J, Yu X and Guo Y 2018 *Adv. Mater.* **30** 1801751

[57] Sathiya M, Rousse G, Ramesha K, Laisa C P, Vezin H, Sougrati M T, Doublet M-L, Foix D, Gonbeau D, Walker W, Prakash A S, Ben Hassine M, Dupont L and Tarascon J M 2013 *Nat. Mater.* **12** 827

[58] Chen J, Yang Y, Tang Y, Wang Y, Li H, Xiao X, Wang S, Darma M S D, Etter M, Missyul A, Tayal A, Knapp M, Ehrenberg H, Indris S and Hua W 2023 *Adv. Funct. Mater.* **33** 2211515

[59] Zhang C, Li Y, Liu Y, Shen X, Hu Z, Chen J M, Lin H J, Chen C T, Kong Q, Hu Y, Gao Y, Haw S C, Wang X, Yu R, Wang Z and Chen L 2024 *Nano Energy* **121** 109254

[60] Lin C, Piao Y, Kan Y, Bareñ J, Bloom I, Ren Y, Amine K and Chen Z 2014 *ACS Appl. Mater. Interfaces* **6** 12692

[61] Luo K, Roberts M R, Hao R, Guerrini N, Pickup D M, Liu Y S, Edström K, Guo J, Chadwick A V, Duda L C and Bruce P G 2016 *Nat. Chem.* **8** 684

[62] Zhou K, Zhang Z, Cao B, Jiao S, Zhu J, Xu X, Chen P, Xiong X, Xu L, Wang Q, Wang X, Yu X and Li H 2025 *Nano Energy* **135** 110639

[63] Li H, Fong R, Woo M, Ahmed H, Seo D H, Malik R and Lee J 2022 *Joule* **6** 53

[64] Zhang Y, Chen Z, Shi X, Meng C, Das P, Zheng S, Pan F and Wu Z S 2023 *Adv. Energy Mater.* **13** 2203045

[65] Wang E, Xiao D, Wu T, Liu X, Zhou Y, Wang B, Lin T, Zhang X and Yu H 2022 *Adv. Funct. Mater.* **32** 2201744